

# RSC Advances



This is an *Accepted Manuscript*, which has been through the Royal Society of Chemistry peer review process and has been accepted for publication.

*Accepted Manuscripts* are published online shortly after acceptance, before technical editing, formatting and proof reading. Using this free service, authors can make their results available to the community, in citable form, before we publish the edited article. This *Accepted Manuscript* will be replaced by the edited, formatted and paginated article as soon as this is available.

You can find more information about *Accepted Manuscripts* in the [Information for Authors](#).

Please note that technical editing may introduce minor changes to the text and/or graphics, which may alter content. The journal's standard [Terms & Conditions](#) and the [Ethical guidelines](#) still apply. In no event shall the Royal Society of Chemistry be held responsible for any errors or omissions in this *Accepted Manuscript* or any consequences arising from the use of any information it contains.

*Synthesis high performance of  $\text{Li}_4\text{Ti}_5\text{O}_{12}$  microspheres and  $\text{TiO}_2$  nanowires from natural ilmenite*

Feixiang Wu, Zhixing Wang\*, Xinhai Li, Huajun Guo

School of Metallurgy and Environment, Central South University, Changsha, 410083, P.R. China.

\*Corresponding author email: zhixing.csu@gmail.com

**Abstract**

The low cost production of Ti-containing nanomaterials from natural resources is an attractive method for producing materials suitable for the growing energy storage industry. In this work, natural ilmenite is transformed into either  $\text{Li}_4\text{Ti}_5\text{O}_{12}$  microspheres or  $\text{TiO}_2$  nanowires through a series of chemical and thermal processes by the cross of metallurgy and material science. The produced well-crystallized  $\text{Li}_4\text{Ti}_5\text{O}_{12}$  microspheres is composed of nanosized particles that show high cycle stability, coulombic efficiencies, and rate capability for  $C$ -rates as high as  $20C$ . The initial discharge capacities are 173.1, 168.5, 167.2, 163.4, 160.0, 155.4 and 142.7  $\text{mAhg}^{-1}$  at the 0.1, 0.5, 1, 2, 5, 10 and 20  $C$  rates, respectively. After 100 cycles, the as-prepared  $\text{Li}_4\text{Ti}_5\text{O}_{12}$  retains 99.1%, 98.9%, 96.8% and 91.8% of its initial discharge capacities at the 2, 5, 10 and 20  $C$  rates, respectively. The synthesized echinus-like anatase  $\text{TiO}_2$  nanowire aggregations also demonstrate excellent cycling performance, even at high current densities.

**Keywords:** Lithium ion batteries; Lithium titanate; Titanium dioxide; Anode material;

---

\*Corresponding author. Tel: +86-731-88836633, Fax: +86-731-88836633  
E-mail address: zhixing.csu@gmail.com (Z.X. Wang).

Ilmenite

## 1. Introduction

Nowadays, development of human society is closely related with the energy, resources and environment. Social development needs of the consumption of energy and resources. Therefore, with the increasing environmental problems caused by conventional energy sources and the gradual depletion of global energy and metallic ore resources, the development of new energy and comprehensive utilization of mineral resources have become the focus of worldwide attention. Electrochemical energy systems, such as batteries and supercapacitors, have garnered significant attention due to their high energy or high power characteristics, often available in small formats. Rechargeable Li-ion batteries are of particular interest for a number of applications ranging from portable electronics to transportation due to their high energy density, high voltage, and ambient temperature operation.<sup>1-5</sup> However, improved performance of current Li-ion batteries is desired to meet higher energy and power requirements.

Graphite is the current industry anode material for Li-ion batteries; however, it has limitations. First, the theoretical capacity is lower than many other materials which can intercalate or alloy with Li. Second, the low potential for lithium intercalation can lead to the lithium plating during charge. Li commonly plates as dendrite which have significant safety concerns. Another issue originates from charge consumption required to form the solid electrolyte interphase (SEI) layer that is essential to electrode stability in terms of the capacity, power retention, and cycle

life.<sup>6-10</sup>

Spinel lithium titanate ( $\text{Li}_4\text{Ti}_5\text{O}_{12}$ ) and anatase titanium dioxide ( $\text{TiO}_2$ ) have been viewed as two promising alternative anode materials to graphite in Li-ion batteries.<sup>11-15</sup> Spinel  $\text{Li}_4\text{Ti}_5\text{O}_{12}$  has a theoretical capacity of  $175 \text{ mAhg}^{-1}$  with high deintercalation reversibility.<sup>16-18</sup> Due to the flat  $\text{Li}^+$  insertion potential  $\sim 1.55 \text{ V}$  for  $\text{Li}_4\text{Ti}_5\text{O}_{12}$ , above the reduction potential of electrolyte solvents, a SEI film will not form on  $\text{Li}_4\text{Ti}_5\text{O}_{12}$ , which may allow for reduced irreversible capacity. Further, as a “zero-strain” insertion material, it has excellent cycling performance. In comparison, anatase  $\text{TiO}_2$  is a fast Li insertion/extraction host with an insertion potential  $\sim 2.0 \text{ V}$ , low volume expansion (3–4%) during lithium insertion, and a high theoretical capacity of  $336 \text{ mAhg}^{-1}$ .<sup>19,20</sup> These features make them two promising anode materials for large-scale long-life energy storage batteries. However, both of them are still away from perfect because of its low electronic conductivity, which limits its rate stability.

Nanostructured  $\text{TiO}_2$  and  $\text{Li}_4\text{Ti}_5\text{O}_{12}$  are conventionally prepared from  $\text{TiO}_2$  or Ti-based organic compounds. Generally, these highly pure raw compounds are prepared from Ti-containing ores or other Ti slag via complex, expensive, energy consuming processes that remove impurities. In this paper, new methods to synthesize nanostructured  $\text{TiO}_2$  and  $\text{Li}_4\text{Ti}_5\text{O}_{12}$  from natural ilmenite ( $\text{FeTiO}_3$ ) through a series of easily replicated processes are proposed:  $\text{TiO}_2$  nanowire synthesis by a high temperature hydrothermal method and  $\text{Li}_4\text{Ti}_5\text{O}_{12}$  microspheres synthesis by spray drying. Natural ilmenite ( $\text{FeTiO}_3$ ) is one of the primary global sources of

titanium dioxide. In China, commercially, pigment grade titanium dioxide is mainly produced by the complex sulfate processes with generation of a large amount of waste acidic iron(II) solutions and  $\text{FeSO}_4 \cdot 7\text{H}_2\text{O}$  waste slag, which causes not only severe environmental problems but also the waste of iron resource. Finally, the obtained pigment grade titanium dioxide was often used to prepared high purity of nanostructured  $\text{TiO}_2$  and organic Ti-contained compounds by using complex metallurgical extraction and materials preparation processes, which are extensively used in coatings, paper, porcelain, plastics, catalysts, cosmetics, gas sensors and energy.

In previous publications, we used hydrochloric acid as a leachant to dissolve mechanically activated ilmenite to obtain a lixivium (or filtrate) which was used to prepare  $\text{LiFePO}_4$ .<sup>21,22</sup> In this process, another product of hydrolyzed titania residue was used to prepare  $\text{Li}_4\text{Ti}_5\text{O}_{12}$  directly after a two-step alkaline leaching.<sup>23</sup> The obtained  $\text{Li}_4\text{Ti}_5\text{O}_{12}$  particles were not uniform and the electrochemical performance was very poor.<sup>23</sup> The obtained hydrolyzed titania residue was hard to use by the chlorination process. Owing to its high chemical activity and reaction with  $\text{H}_2\text{O}_2$  and  $\text{NH}_3 \cdot \text{H}_2\text{O}$ , Ti could be easily and selectively extracted from the high Ti-containing residue by alkaline-hydrogen peroxide leaching.<sup>24</sup> The lixivium from hydrolyzed titania residue was used to synthesize  $\text{TiO}_2$  nanosheets from which  $\text{Li}_4\text{Ti}_5\text{O}_{12}$  was prepared; however, the performance was poor and this method consumed significant  $\text{LiOH}$ .<sup>25</sup>

In this work, we combine the metallurgical extraction and materials preparation

together to develop a series of short processes to synthesize Li-ion battery anode materials  $\text{TiO}_2$  and  $\text{Li}_4\text{Ti}_5\text{O}_{12}$  from natural ilmenite. In this method,  $\text{TiO}_2$  does not need to be prepared from lixivium of ammonia titanium peroxide solution, as in previous work.<sup>25</sup> Here, only  $\text{LiOH}$  was added into the lixivium to obtain a lithium (ammonia) titanium peroxide solution which was used to prepare  $\text{Li}_4\text{Ti}_5\text{O}_{12}$  microspheres. Additionally, the addition of  $\text{NaOH}$  to the lixivium of ammonia titanium peroxide solution has a profound significance of not only decreasing the content of  $\text{SiO}_2$  in the  $\text{TiO}_2$ , but also forming uniform  $\text{TiO}_2$  nanowires.

The major element of Ti in ilmenite is utilized to prepare high performance  $\text{TiO}_2$  and  $\text{Li}_4\text{Ti}_5\text{O}_{12}$  which can be used in Li-ion batteries. The produced  $\text{Li}_4\text{Ti}_5\text{O}_{12}$  microspheres show very good performance, even better than our results by using analytically pure and organic titanium compounds.<sup>26,27</sup> The produced  $\text{TiO}_2$  nanowires also show good performance and high purity. Thus, through these methods, stable Li-ion materials can be synthesized using processes that reduce redundancy, reduce the cost of production, and reduce the negative environmental impact from the hazardous waste slag and acid to environment.

## 2. Experimental

### 2.1. Materials

The as-received 100–200  $\mu\text{m}$  ilmenite particles consisted of several metal oxides (Table 1) and were used as the raw material.

**Table 1** Chemical composition of the ilmenite (wt.%)

$\text{TiO}_2$	$\text{FeO}$	$\text{Fe}_2\text{O}_3$	$\text{MgO}$	$\text{SiO}_2$	$\text{Al}_2\text{O}_3$	$\text{CaO}$	$\text{MnO}_2$
----------------	--------------	-------------------------	--------------	----------------	-------------------------	--------------	----------------

47.60	32.81	7.25	5.64	3.35	1.66	0.70	0.663
-------	-------	------	------	------	------	------	-------

## 2.2. Experimental method and experimental procedure

Detailed illustration of the synthesis process of spherical  $\text{Li}_4\text{Ti}_5\text{O}_{12}$  and nanowires  $\text{TiO}_2$  from natural ilmenite is shown in Fig.1.

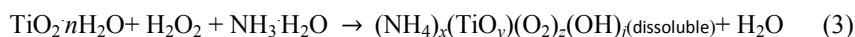
### 2.2.1 lixivium of ammonia titanium peroxide solution

Compounds of Ti and Fe were effectively separated by hydrochloric acid leaching of natural ilmenite following equations (1) and (2). The obtained hydrolyzed titania residue and Fe-rich filtrate were prepared following previously reported methods.<sup>21, 22, 24</sup> According to the previous results, Ti and Si were directionally enriched in hydrolyzed titania residue, meanwhile, Fe, Mg, Al, Mn and Ca were dissolved in the iron-rich filtrate.



The lixivium of ammonia titanium peroxide solution was prepared by alkaline-hydrogen peroxide leaching of hydrolyzed titania residue via methods previously reported.<sup>24, 25</sup> The hydrolyzed titania residue powder (5 g) was placed in a 500 ml round-bottomed flask attaching to a refluxing condenser. 10 wt.% ammonia solution (60 g) was added in the flask and white slurry was observed. The white slurry was maintained at 35 °C in a thermostatically controlled water bath, equipped with a digitally controlled thermometer (within  $\pm 2^\circ\text{C}$ ). Hydrogen peroxide solutions containing 10 wt.%  $\text{H}_2\text{O}_2$  (180g) was then added to the white slurry to react with Ti under vigorous stirring of 300 rpm. After 20 min, the solution was rapidly cooled and

filtered, and then aqueous ammonia titanium peroxide solution was obtained according to equation (3).

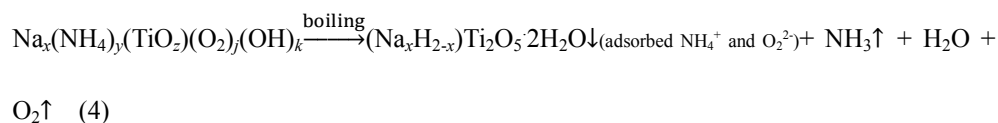


### 2.2.2 Synthesis of $\text{Li}_4\text{Ti}_5\text{O}_{12}$ microspheres

$\text{LiOH} \cdot \text{H}_2\text{O}$  and lixivium of ammonia titanium peroxide (0.816 Li:Ti molar ratio) solutions were mixed and stirred for 10 min to form lithium (ammonia) titanium peroxide solution. The prepared lithium (ammonia) titanium peroxide solution was added into a spray dryer machine by peristaltic pump at  $300 \text{ ml} \cdot \text{h}^{-1}$ . The homogenous solution was atomized at  $200 \text{ }^\circ\text{C}$  using a two-fluid nozzle with an atomizing pressure of 0.2 MPa. The spray-dried precursor powders were further calcined in air at  $675 \text{ }^\circ\text{C}$  for 16 h to form  $\text{Li}_4\text{Ti}_5\text{O}_{12}$  particles.

### 2.2.3 Synthesis of $\text{TiO}_2$ nanowires

$\text{NaOH}$  solution was added into the obtained lixivium of ammonia titanium peroxide solution to form a 8:1 Na:Ti molar ratio. The obtained aqueous sodium (ammonia) titanium peroxide solution was heated to boiling point with vigorous stirring in an oil bath. After 1 h, according to equation (4), precipitation of titanium dioxide hydrate with nanosized  $\text{TiO}_2$  crystals was obtained and subsequently washed by 2 wt.%  $\text{HNO}_3$  several times. The  $\text{TiO}_2$  precipitation was dried in an oven at  $80 \text{ }^\circ\text{C}$  to obtain titanium dioxide hydrate powder which was calcined at  $300 \text{ }^\circ\text{C}$  for 3 h to form  $\text{TiO}_2$  particles.



### 2.3. Analysis

Micrographs of the prepared powders were taken with a field-emission LEO 1530 microscope (Zeiss, Germany) at a working distance of 3-6 mm and accelerating field of 2-3 kV and transmission electron microscope (TEM) (Tecnai G12, Netherlands). Powder composition was measured using energy-dispersive X-ray spectroscopy (EDS). The elemental contents of solutions and samples were analyzed using inductively coupled plasma (ICP) emission spectroscopy (IRIS intrepid XSP, Thermo Electron Corporation, Japan). Powder X-ray diffraction (XRD) (Rint-2000, Rigaku, Japan) using Cu K $\alpha$  radiation was employed to identify the crystalline phase of the synthesized materials. The specific surface area of the produced materials ( $S_{\text{BET}}$ ) was calculated from N<sub>2</sub> adsorption isotherms using the Brunauer-Emmett-Teller equation in the range of relative pressures from 0.02 to 0.3. XPS analysis was performed using a Al K $\alpha$  source (Thermo, USA).

14 mm diameter electrodes with typical mass loadings of 1.95–2mg/cm<sup>2</sup> were tested in 2025-type coin cells versus metallic Li. The produced electrodes were composed of 80 wt.% Li<sub>4</sub>Ti<sub>5</sub>O<sub>12</sub> (or TiO<sub>2</sub>) powders, 10 wt.% carbon black, and 10 wt.% poly(vinylidene fluoride) as binder. After mixing in N-methyl pyrrolidinone, the slurry was uniformly cast on a thin copper foil and dried in vacuum for 12 h at 120 °C. An electrolyte of LiPF<sub>6</sub> in carbonates (EC:EMC:DMC = 1:1:1 by volume) was used. A polypropylene separator was used. Cells were assembled in a dry argon-filled glove box and were charged and discharged at room temperature over voltage ranges of 1.0–2.5 V and 1.0-3.0 V for Li<sub>4</sub>Ti<sub>5</sub>O<sub>12</sub> and TiO<sub>2</sub> versus Li/Li<sup>+</sup>,

respectively.

### 3. Results and discussion

#### 3.1 $\text{Li}_4\text{Ti}_5\text{O}_{12}$ microspheres

The XRD pattern of the precursor of  $\text{Li}_4\text{Ti}_5\text{O}_{12}$  has no peaks, indicating no appearance of crystalline phases (Figure 2a). The as-prepared  $\text{Li}_4\text{Ti}_5\text{O}_{12}$  is single-phase spinel lithium titanium oxide (cubic phase, space group  $Fd-3m$ ) in accordance with spinel  $\text{Li}_4\text{Ti}_5\text{O}_{12}$  (JCPDS Card No. 49-0207) and well crystallized. Thus, well crystallized, single phase  $\text{Li}_4\text{Ti}_5\text{O}_{12}$  can be synthesized at relatively low temperature (675 °C) by calcining the precursor prepared by this method. Prior to heat treatment, the precursor powders are characterized by the spherical morphology with a diameter size of about 1-5  $\mu\text{m}$ . From Fig.2 (b and c), the surface of the precursor is smooth, which has been magnified in Fig.2 (d). The microspheres particles contain lots of nanoparticles with size of several nanometers (5 nm) which is attributed to decomposition of hydrogen peroxide and ammonia solution in the spray process. Owing to lithium titanium peroxide aqueous solution (We added the solution of LiOH into the lixivium of ammonia titanium peroxide which is from the leach of hydrolyzed titania residue by using alkaline-hydrogen peroxide leaching method.) in which the metal ions are ion-level homogeneously mixed, we got a uniform precursor of  $\text{Li}_4\text{Ti}_5\text{O}_{12}$  microspheres with homogeneous mixing of Li and Ti ions. Owing to the effect of these nanoscale and uniform particles,  $\text{Li}_4\text{Ti}_5\text{O}_{12}$  could be obtained at relatively low calcination temperature with no impurities of  $\text{Li}_2\text{TiO}_3$  or  $\text{TiO}_2$ . There is no obvious circle in the SAED pattern indicating no appearance of crystalline phases

(Fig.2 d), which is well in accordance with the XRD result of precursor. In Fig.2 (e) and Fig.3 (a and f), after calcination at 675°C for 16 h, the as-prepared  $\text{Li}_4\text{Ti}_5\text{O}_{12}$  also shows uniform and spherical structure morphology with the same size as the precursor. However, owing to the decomposition of precursor, the surface of microspheres changes into rough and porous surface which is constituted with aggregations of nanoparticles with the size of about 100-200 nm. The as-prepared  $\text{Li}_4\text{Ti}_5\text{O}_{12}$  have a measured  $S_{\text{BET}}$  of  $10.3 \text{ m}^2 \cdot \text{g}^{-1}$  (Fig. 2f), which is consistent with an average  $\text{Li}_4\text{Ti}_5\text{O}_{12}$  particle size of  $\sim 170 \text{ nm}$ , assuming  $\text{Li}_4\text{Ti}_5\text{O}_{12}$  density to be  $1.68 \text{ g} \cdot \text{cm}^{-3}$  and smooth particle surface. From the EDS pattern of selective area in the TEM image Fig.3 (f), little impurity of Si has been detected in the synthetic  $\text{Li}_4\text{Ti}_5\text{O}_{12}$ . Due to the weak alkaline condition of leaching, a little Si in the hydrolyzed titania residue is dissolved. From EDS mapping of the  $\text{Li}_4\text{Ti}_5\text{O}_{12}$  (Fig.3 b, c, d and e), the Si is well-distributed in the as-produced  $\text{Li}_4\text{Ti}_5\text{O}_{12}$ . Because the Si and Fe which are from natural ilmenite could be the most likely impurities in as-produced  $\text{Li}_4\text{Ti}_5\text{O}_{12}$ , we performed high-resolution X-ray photoelectron spectroscopy (XPS) including Fe scan and Si scan on as-produced  $\text{Li}_4\text{Ti}_5\text{O}_{12}$  to know the impurity well (Fig.3g). The XPS results show only Si as impurity in as-produced  $\text{Li}_4\text{Ti}_5\text{O}_{12}$ . Fig.3 (i) shows the HRTEM images of as-prepared  $\text{Li}_4\text{Ti}_5\text{O}_{12}$  nanoparticles. As can be seen, there is a lattice fringe with a lattice spacing of about 0.48 nm, corresponding to (1 1 1) interplanar spacing of  $\text{Li}_4\text{Ti}_5\text{O}_{12}$ , which indicates the well-crystallized spinel phase in the nanostructured materials prepared from relatively low temperature heat treatment. The SAED pattern in Fig.3 (i), with several marked rings corresponding to  $\text{Li}_4\text{Ti}_5\text{O}_{12}$

(1 1 1), (3 1 1), (4 0 0) and (4 4 0) planes, can be indexed to spinel  $\text{Li}_4\text{Ti}_5\text{O}_{12}$  with the cubic space group  $Fd-3m$ .

The voltage profiles of  $\text{Li}_4\text{Ti}_5\text{O}_{12}$  microspheres at room temperature in charge-discharge test at various current densities are shown in Fig.4. The cell was first cycled at  $C/10$  for 3 cycles,  $C/2$  for 5 cycles,  $1C$  for 50 cycles,  $2C$  for 100 cycles,  $5C$  for 100 cycles,  $10C$  for 100 cycles,  $20C$  for 100 cycles and then turned to  $0.1C$  for 10 cycles. At all  $C$ -rates, the charge/discharge curves exhibit a long and flat voltage plateaus. In the first discharge process, the as-prepared  $\text{Li}_4\text{Ti}_5\text{O}_{12}$  electrode exhibits a remarkably high initial discharge capacity at  $0.1C$  rate, up to  $173.1 \text{ mAhg}^{-1}$ , which is almost equal to its theoretical capacity ( $175 \text{ mAhg}^{-1}$ ). The subsequent  $\text{Li}^+$  extraction, proceeding up to  $2.5 \text{ V}$ , shows a capacity of  $170.2 \text{ mAhg}^{-1}$ , with a high coulombic efficiency (ratio of extraction to insertion capacity) of  $98.32\%$ . By increasing the  $C$ -rate, the cell shows  $168.5$ ,  $167.2$ ,  $163.4$ ,  $160.0$ ,  $155.4$  and  $142.7 \text{ mAhg}^{-1}$  at  $0.5$ ,  $1$ ,  $2$ ,  $5$ ,  $10$  and  $20 C$  rates, respectively. The capacities at all charge/discharge rates are much larger than other  $\text{Li}_4\text{Ti}_5\text{O}_{12}$  and  $\text{Li}_4\text{Ti}_5\text{O}_{12}/\text{C}$  electrodes made by chemically pure or analytically pure Titanium compounds.<sup>26-44</sup> Moreover, the cycling performance of as-prepared  $\text{Li}_4\text{Ti}_5\text{O}_{12}$  is shown in Fig.4 (b). As shown, the cycling curves of discharge and charge are coincided with each other, indicating a high coulombic efficiency in the charge/discharge of this cell. At all the current densities, after 50 or 100 cycles, the as-prepared  $\text{Li}_4\text{Ti}_5\text{O}_{12}$  electrode retains  $97.9\%$ ,  $99.1\%$ ,  $98.9\%$ ,  $96.8\%$  and  $91.8\%$  of its initial discharge capacities at the  $1$ ,  $2$ ,  $5$ ,  $10$  and  $20 C$  rates, respectively. In the last 10 cycles at  $C/10$  rate, the charge capacity of  $459^{\text{th}}$  retains

103.9% of 468<sup>th</sup> charge capacity. The excellent electrochemical performance might be attributed to as-prepared  $\text{Li}_4\text{Ti}_5\text{O}_{12}$  microspheres obtained by this novel method and natural ilmenite. The as-produced  $\text{Li}_4\text{Ti}_5\text{O}_{12}$  microspheres composed of nanoparticles around 100 nm contained rough surface and inside pores. These nanosized  $\text{Li}_4\text{Ti}_5\text{O}_{12}$  particles connected with each other forming interconnected  $\text{Li}_4\text{Ti}_5\text{O}_{12}$  nano-network which provide massive interface among nanoparticles and can be the bridge for electron and  $\text{Li}^+$  transport through shorter path within and between the nano-particles. Meanwhile, the inside pores make a larger electrode–electrolyte contact area for  $\text{Li}^+$  insertion/extraction in the rough and porous spherical particles. Therefore, the as-prepared  $\text{Li}_4\text{Ti}_5\text{O}_{12}$  shows excellent high-rate and cycling performance, which is better than our previous  $\text{Li}_4\text{Ti}_5\text{O}_{12}$  microspheres obtained by chemically pure or analytically pure titanium compounds (Table.2).

Fig.4 (c) shows the first and 468<sup>th</sup> charge/discharge curves of  $\text{Li}_4\text{Ti}_5\text{O}_{12}$  at  $C/10$  rate. After total 450 cycles at miscellaneous current densities, the cell returns to  $C/10$  and still keeps a remarkably high discharge capacity of  $168.8\text{mAhg}^{-1}$  which is 97.6 % of the initial discharge capacity at  $0.1C$ -rate. As can be seen in Fig.4 (d), all of the five cycles have a sharp pair of cathodic/anodic peaks centered at 1.50V and 1.63V, corresponding to the lithium insertion/extraction in spinel  $\text{Li}_4\text{Ti}_5\text{O}_{12}$  lattice, which are in accordance with the plateaus of the discharging/charging curves. The measured value of the ratio for peak currents  $i_{pa}/i_{pc}$  is nearly 1, and the integral voltammetric area of the discharging/charging branches is almost equal. Moreover, after 471 cycles, 5 cyclic voltammograms are coincided with each other, indicating a very perfect

coulombic efficiency. After comparing the SEM images of electrodes before and after cycling in Fig.4 (e and f), the nano-micron structure is still maintained and stable after ~500 cycles, which is due to the “zero-strain” during charge and discharge. As the results of Fig.4, this  $\text{Li}_4\text{Ti}_5\text{O}_{12}$  shows a very steady-going structure, high capacities and high cycling performance even after hundreds of cycles at high C-rates.

### 3.2 $\text{TiO}_2$ nanowires

Fig.2 (a) shows the XRD patterns of the precursor and as-prepared  $\text{TiO}_2$ . The precursor shows weak (1 0 1) and (2 0 0) diffraction peaks of anatase  $\text{TiO}_2$ . After calcination at 300 °C for 3 h, the as-prepared  $\text{TiO}_2$  with high crystallinity is well ascribed to the (1 0 1), (1 1 0), (2 0 0), (2 1 1), (2 0 4), (1 1 6) and (2 1 5) diffraction peaks of anatase  $\text{TiO}_2$ . It indicates that the structure of the precursor is easy to change into anatase  $\text{TiO}_2$  nanowires. ICP analysis reveals that content percents of  $\text{SiO}_2$  and  $\text{TiO}_2$  in synthetic  $\text{TiO}_2$  are 0.32% and 99.68%. Other elements like Mg, Fe, Al, Mn and Na are not detected by AAS and ICP in the as-prepared  $\text{TiO}_2$ . In our earlier work, the content percents of  $\text{SiO}_2$  and  $\text{TiO}_2$  in synthetic  $\text{TiO}_2$  are 2.19% and 97.81% and the content percent of  $\text{TiO}_2$  in nanosheets  $\text{TiO}_2$  is 99.31%.<sup>24, 25</sup> Therefore, the addition of NaOH before the boiling process can decrease the content percent of  $\text{SiO}_2$  in the as-prepared  $\text{TiO}_2$ . The NaOH can react with silicon in the leaching solution to form  $\text{SiO}_3^{2-}$  ion which can exist stably in the alkaline solution. We also detect elements on the surface of samples by EDS. As shown in Fig.5 (d), only little Si is detected in as-prepared  $\text{TiO}_2$ , which are consistent with the ICP results.

When boiling the sodium titanium peroxide solution, the  $\text{H}_2\text{O}_2$  is gradually decomposed. Due to the interfacial tension, van der Waals attractive forces, and other factors, the titanate nucleus would aggregate together to form “multi-nuclei”. Subsequently, the titanate “multi-nuclei” gradually grow up and assemble into a micro spherical shape along with  $\text{H}_2\text{O}_2$  decomposition. The precursor is calcined at  $300\text{ }^\circ\text{C}$  for 3 h to synthesize anatase  $\text{TiO}_2$ . As shown in Fig.2 (g, h and i), the morphology images of the precursor and as-prepared  $\text{TiO}_2$  are the similar echinus-like structure with a diameter about  $0.5\text{-}1.5\mu\text{m}$ , which shows high BET SSA of  $20.2\text{m}^2/\text{g}$ . As-prepared  $\text{TiO}_2$  maintains the morphology of the precursor, which is attributed to the low calcined temperature. The enlarged image of the particles of as-prepared  $\text{TiO}_2$  in Fig.5 (a) shows that the spherical particles or microspheres are composed of aggregations of nanowires, which are consistent with the TEM images (Fig.5 (b and c)). As shown in Fig.5 (b and c), the morphology images of as-prepared  $\text{TiO}_2$  are the echinus-like structure with aggregations of nanowires. These nanowires are acicula-shaped with the diameter in the range of  $14.4\text{ nm}$  and the length is about  $200\text{-}500\text{ nm}$ . From Fig.2 (g), there is no obvious circle in the inset SAED pattern indicating no appearance of crystalline phases, which is well in accordance with the XRD result of precursor. However, the SAED pattern in Fig.5 (e), with several marked rings corresponding to  $\text{TiO}_2$  (1 0 1), (0 0 4), (2 0 0) and (2 1 1) planes, can be indexed to anatase  $\text{TiO}_2$  (JCPDS Card No. 65-5714). Fig.5 (f) shows the HRTEM images of as-prepared  $\text{TiO}_2$  nanoparticles. As can be seen, there is a lattice fringe with a lattice spacing of about  $3.51\text{ \AA}$ , corresponding to (1 0 1) inter planar spacing of

TiO<sub>2</sub>, which indicates the well-crystallized anatase phase in the nanostructured materials. The inset SAED patterns are obtained by Fourier transformation in the selected area of HRTEM images. The inset FFT image in Fig.5 (f) also gives a sharp spot corresponding to the (1 0 1) plane of anatase TiO<sub>2</sub>.

Fig.6 (a) shows the initial three potential-capacity profiles of anatase TiO<sub>2</sub> at the current density of 20 mA g<sup>-1</sup>. In these three cycles, the charge/discharge curves exhibit a long and flat voltage plateaus at about 1.77 and 1.88 V for discharging and charging, respectively. In the first discharge process, anatase TiO<sub>2</sub> shows 291.9 mAh g<sup>-1</sup> at a current density of 20 mA g<sup>-1</sup>. The subsequent Li<sup>+</sup> extraction of anatase TiO<sub>2</sub> shows a capacity of 248.2 mAh g<sup>-1</sup>. It displays a relative low coulombic efficiency (ratio of extraction to insertion capacity) and a large irreversible capacity. However, in the subsequent two cycles, the discharge/charge curves are gradually coincided with each other, indicating a lower irreversible capacity and a higher coulombic efficiency. The fade of the curve between the first and subsequent cycles shows the large irreversible process after the insertion of Li into TiO<sub>2</sub> anatase structure. This phenomenon is tentatively ascribed to the side reaction of trace surface adsorbed water because of the large specific surface area. The trace water in the anatase TiO<sub>2</sub> could react irreversibly with lithium forming Li<sub>2</sub>O on inside the inter layers or on surface, which is the major reason for the larger capacity loss. The discharging/charging tends to be stabilized in the following cycles, because the binding water is consumed gradually during the first several cycles.<sup>45, 46</sup> Fig.6 (b) shows the CV pattern of anatase TiO<sub>2</sub> electrodes. Three cathodic peak of lithium insertion can be found in the voltammogram near 1.50,

1.55, and 1.71 V vs.  $\text{Li}^+/\text{Li}$ ; meanwhile, three anodic peaks of lithium extraction at 1.55, 1.67, and 2.03 V vs.  $\text{Li}^+/\text{Li}$  are observed. The sharp pair of peaks (1.71 and 2.03 V) appears to the lithium insertion/extraction in anatase  $\text{TiO}_2$  lattice, which are in accordance with the plateaus of the discharging/charging curves in Fig.6 (a). While other two pairs at the lower potential region are the characteristic of capacitive charging process, which may represent a different mechanism of lithium intercalation into the  $\text{TiO}_2$  host.<sup>45</sup>

Fig.7 (a) shows the discharge and charge capacities of  $\text{TiO}_2$  at the different current densities. The cell was first cycled at  $20 \text{ mA g}^{-1}$  for 3 cycles,  $100 \text{ mA g}^{-1}$  for 5 cycles,  $200 \text{ mA g}^{-1}$  for 20 cycles,  $400 \text{ mA g}^{-1}$  for 50 cycles,  $1000 \text{ mA g}^{-1}$  for 100 cycles,  $2000 \text{ mA g}^{-1}$  for 100 cycles and then turned to  $20 \text{ mA g}^{-1}$  for 10 cycles. At all current densities, the charge/discharge curves exhibit an obvious and flat voltage plateaus. The initial discharge capacities of  $\text{TiO}_2$  are 291.9, 230.9, 222.6, 202.7, 177.3 and  $142.6 \text{ mA h g}^{-1}$  at the current densities of 20, 100, 200, 400, 1000 and  $2000 \text{ mA g}^{-1}$ , respectively. Moreover, the cycling performance of  $\text{TiO}_2$  is shown in Fig.7 (b). As shown, the  $\text{TiO}_2$  shows a very excellent cycling performance. After 20 cycles, the  $\text{TiO}_2$  retains 96.8% of the initial charge capacity at the current densities of  $200 \text{ mA g}^{-1}$ . At the current density of  $400 \text{ mA g}^{-1}$ , the  $\text{TiO}_2$  retains 95.6% of the initial charge capacity after 50 cycles. After 100 cycles, the  $\text{TiO}_2$  retains 91.9% and 86.9% of the initial charge capacities at the current densities of 1000 and  $2000 \text{ mA g}^{-1}$ , respectively. Compared to the previous  $\text{TiO}_2$  nanowires prepared by same method using organic titanium compounds, the

produced TiO<sub>2</sub> nanowires in this work show better rate performance in Table 3 (We can not compare the cycling performance due to the different cycling program). Fig.7 (c) shows the second and 288<sup>th</sup> charge/discharge curves of anatase TiO<sub>2</sub> at the current density of 20mA g<sup>-1</sup>. After total 270 cycles at 200, 400, 1000 and 2000mA g<sup>-1</sup>, the cell returns to 20mA g<sup>-1</sup> and still exhibits a remarkably high discharge capacity of 227.3 mA h g<sup>-1</sup> which is 89.3 % of the second discharge capacity at 20mA g<sup>-1</sup>. As the results of Fig.7, the anatase TiO<sub>2</sub> prepared by natural ilmenite shows a very steady-going structure, high capacities and high cycling performance even after hundreds of cycles at high current densities.

#### 4. Conclusions

In summary, we have reported a successful preparation of uniform Li<sub>4</sub>Ti<sub>5</sub>O<sub>12</sub> microspheres and TiO<sub>2</sub> nanowires from ilmenite *via* easily replicated chemical and thermal methods. Both of the materials are directly produced from the lixivium of ammonia titanium peroxide solution which is the metallurgical-middle product of natural ilmenite. Both of the synthesized materials demonstrate electrochemical performance that exceeds previously reported data for Li<sub>4</sub>Ti<sub>5</sub>O<sub>12</sub> and TiO<sub>2</sub> nanowires made by chemically pure or analytically pure titanium compounds. The Li<sub>4</sub>Ti<sub>5</sub>O<sub>12</sub> microspheres particles demonstrate excellent high rate cycling and stable performance. The echinus-like structure of aggregations of acicula-shaped TiO<sub>2</sub> nanowires also shows good electrochemical performance. The cost of them is competitive with the market price for the same chemicals prepared from primary resources. We believe that this method is a simple, efficient and economical way for both ilmenite utilization and

materials preparation.

### Acknowledgement

Support from the Hunan Provincial Innovation Foundation for Postgraduates (CX2012A004), China Scholarship Council (201206370083), Young Scholarship Award for doctoral candidate funded by Ministry of Education (1343-76140000019), and the National Basic Research Program of China (2014CB643406) are acknowledged.

### Notes and references

- 1 N. Nitta and G. Yushin, *Part. Part. Syst. Char.*, 2014, 4 , 317.
- 2 L. W. Ji, Z. Lin, M. Alcoutlabi and X. W. Zhang, *Energy Environ. Sci.*, 2011, 4, 2682.
- 3 M. Armand and J. M. Tarascon, *Nature*, 2008, 451, 652.
- 4 A. S. Aricò, P. Bruce, B. Scrosati, J. M. Tarascon and W. V. Schalkwijk, *Nat. Mater.*, 2005, 4, 366.
- 5 P. G. Bruce, B. Scrosati and J. M. Tarascon, *Angew. Chem. Int. Ed.*, 2008, 47, 2930.
- 6 H. Yang, H. J. Bang, K. Amine and J. Prakash, *J. Electrochem. Soc.*, 2005, 152, A73.
- 7 H. Yang, S. Amiruddin, H. J. Bang, Y. K. Sun and J. Prakash, *J. Ind. Eng. Chem.*, 2006, 12, 12.
- 8 H. Yang and X. D. Shen, *J. Power Sources*, 2007, 167, 515.
- 9 M. Lu, H. Cheng and Y. Yang, *Electrochim. Acta*, 2008, 53, 3539.
- 10 R. Fong, U. von Sacken and J. R. Dahn, *J. Electrochem. Soc.*, 1990, 137, 2009.
- 11 T. Ohzuku, A. Ueda and N. Yamamoto, *J. Electrochem. Soc.*, 1995, 142, 1431.
- 12 S. I. Pyun, S. W. Kim and H. C. Shin, *J. Power Sources*, 1999, 81, 248.

- 13 J. Gao, C.Y. Jiang, J.R. Ying and C. R. Wan, *J. Power Sources*, 2006, 155, 364.
- 14 Y. G. Guo, Y. S. Hu and J. Maier, *Chem. Commun.*, 2006, 2783.
- 15 M. Wagemaker, W. J. H. Borghols and F. M. Mulder, *J. Am. Chem. Soc.*, 2007, 129, 4323.
- 16 K. Zaghib, M. Simoneau, M. Armand and M. Gauthier, *J. Power Sources*, 1999, 81, 300.
- 17 S. Ma and H. Noguchi, *J. Electrochem.Soc.*, 2001, 148, 589.
- 18 D. Peramunage and K. M. Abraham, *J. Electrochem. Soc.*, 1998, 145, 2609.
- 19 H. Qiao, L. F. Xiao and L. Z. Zhang, *Electrochem.Comm.*, 2008, 10, 616.
- 20 B. L. He, B. Dong and H. L. Li, *Electrochem. Commun.*, 2007, 9, 425.
- 21 L. Wu, X. H. Li, Z. X. Wang, X. J. Wang, L. J. Li, J. Fang, F. X. Wu and H. J. Guo, *Powder Technol.*, 2010, 199, 293.
- 22 L. Wu, X. H. Li, Z. X. Wang, H. J. Guo, X. J. Wang, F. X. Wu, J. Fang, Z. G. Wang and L. J. Li, *J. Alloys Compd.*, 2010, 506, 271.
- 23 X. J. Wang, X. H. Li, Z. X. Wang, L. Wu, P. Yue, H. J. Guo, F. X. Wu and T. T. Ma, *Powder Technol.*, 2010, 204, 198.
- 24 F. X. Wu, X. H. Li, Z. X. Wang, L. Wu, H. J. Guo, X. H. Xiong, X. P. Zhang and X. J. Wang, *Int. J. Miner. Process.*, 2011, 98, 106.
- 25 F. X. Wu, X. H. Li, Z. X. Wang, H. J. Guo, L. Wu, X. H. Xiong and X. J. Wang, *Powder Technol.*, 2011, 213, 192.
- 26 F. X. Wu, X. H. Li, Z. X. Wang, H. J. Guo, Z. J. He, Q. Zhang, X. H. Xiong and P. Yue, *J. Power Sources*, 2012, 202, 374.
- 27 F. X. Wu, Z. X. Wang, X. H. Li, H. J. Guo, P. Yue, X. H. Xiong, Z. J. He and Q. Zhang, *Electrochim. Acta*, 2012, 78, 331.

- 28 H. Yan, Z. Zhu, D. Zhang, W. Li and Q. Lu, *J. Power Sources*, 2012, 219, 45.
- 29 R. Cai, S. M. Jiang, X. Yu, B. T. Zhao, H. T. Wang and Z. P. Shao, *J. Mater. Chem.*, 2012, 22, 8013.
- 30 Y. J. Bai, C. Gong, Y. X. Qi, N. Lun and J. Feng, *J. Mater. Chem.*, 2012, 22, 19054.
- 31 B. H. Li, C. P. Han, Y. B. He, C. Yang, H. D. Du, Q. H. Yang and F. Y. Kang, *Energy Environ. Sci.*, 2012, 5, 9595.
- 32 G. Y. Liu, H. Y. Wang, G. Q. Liu, Z. Z. Yang, B. Jin and Q. C. Jiang, *J. Power Sources*, 2012, 220, 84.
- 33 H. F. Ni and L. Z. Fan, *J. Power Sources*, 2012, 214, 195.
- 34 H. G. Jung, S. T. Myung, C. S. Yoon, S. B. Son, K. H. Oh, K. Amine, B. Scrosati and Y. K. Sun, *Energy Environ. Sci.*, 2011, 4, 1345.
- 35 J. Wolfenstine and J. L. Allen, *J. Power Sources*, 2008, 180, 582.
- 36 X. Li, M. Z. Qu, Y. J. Huai and Z. L. Yu, *Electrochim. Acta*, 2010, 55, 2978.
- 37 C. M. Shen, X. G. Zhang, Y. K. Zhou and H. Li, *Mater. Chem. Phys.*, 2002, 78, 437.
- 38 K. C. Hsiao, S. C. Liao and J. M. Chen, *Electrochim. Acta*, 2008, 53, 7242.
- 39 S. H. Ju and Y. C. Kang, *J. Phys. Chem. Sol.*, 2009, 70, 40.
- 40 D. Yoshikawa, Y. Kadoma, J. M. Kim, K. Ui, N. Kumagai, N. Kitamura and Y. Idemoto, *Electrochim. Acta*, 2010, 55, 1872.
- 41 J. Z. Chen, L. Yang, S. H. Fang and Y. F. Tang, *Electrochim. Acta*, 2010, 55, 6596.
- 42 Y. F. Tang, L. Yang, Z. Qiu and J. S. Huang, *Electrochem. Commun.*, 2008, 10, 1513.
- 43 X. Guo, H. F. Xiang, T. P. Zhou, W. H. Li, X. W. Wang, J. X. Zhou and Y. Yu, *Electrochim. Acta*, 2013, 109, 33.

44 Y. Wang, H. B. Rong, B. Z. Li, L.D. Xing, X. P. Li and W. S. Li, *J. Power Sources*, 2014, 246, 213.

45 J. R. Li, Z. L. Tang and Z. T. Zhang, *Electrochem. Solid-State Lett.*, 2005, 8, A316.

46 Y. F. Wang, M. Y. Wu and W. F. Zhang, *Electrochim. Acta.*, 2008, 53, 7863.

47 F. X. Wu, Z. X. Wang, X. H. Li and H. J. Guo, *J. Mater. Chem.*, 2011, 21, 12675.

### Figure captions

**Fig.1** The detailed illustration of the synthesis process.

**Fig.2** (a) XRD patterns of the precursors and synthesized  $\text{Li}_4\text{Ti}_5\text{O}_{12}$  and  $\text{TiO}_2$ ; (b) SEM image of the precursor of  $\text{Li}_4\text{Ti}_5\text{O}_{12}$ ; (c and d) TEM images of the precursor of  $\text{Li}_4\text{Ti}_5\text{O}_{12}$  (inset: SAED pattern of the precursor of  $\text{Li}_4\text{Ti}_5\text{O}_{12}$ .); (e) The SEM image of as-prepared  $\text{Li}_4\text{Ti}_5\text{O}_{12}$ ; (f) SEM image and SAED (inset) of the precursor of  $\text{TiO}_2$ ; (g) SEM image of synthesized  $\text{TiO}_2$ . Physisorption isotherms for synthesized (h)  $\text{TiO}_2$  and (i)  $\text{Li}_4\text{Ti}_5\text{O}_{12}$ .

**Fig.3.** SEM (a), EDS mapping (b, c, d and e) and TEM (f) images of as-prepared  $\text{Li}_4\text{Ti}_5\text{O}_{12}$ ; (g) Typical XPS spectra of as-produced  $\text{Li}_4\text{Ti}_5\text{O}_{12}$  (The insets show high-resolution  $\text{Fe}_{2p}$  and  $\text{Si}_{2p}$  spectrums); (h) EDS pattern of selective area in TEM image; (i) HRTEM image and SAED (inset) image of as-produced  $\text{Li}_4\text{Ti}_5\text{O}_{12}$ .

**Fig.4.** (a) Charge/discharge curves of  $\text{Li}_4\text{Ti}_5\text{O}_{12}$  at multiple  $C$ -rates in the voltage range of 1.0-2.5 V; (b) cycling performance of  $\text{Li}_4\text{Ti}_5\text{O}_{12}$  at multiple  $C$ -rates; (c) The first and 468<sup>th</sup> charge/discharge curves of  $\text{Li}_4\text{Ti}_5\text{O}_{12}$  at  $C/10$  rate; (d) Cyclic voltammograms of the as-prepared  $\text{Li}_4\text{Ti}_5\text{O}_{12}$  at the scan rate of  $0.1 \text{ mVs}^{-1}$  between 2.5 and 1 V after charge/discharge testing; SEM images of as-produced  $\text{Li}_4\text{Ti}_5\text{O}_{12}$

electrodes (e) before and (f) after cycling.

**Fig.5** (a) SEM image of as-prepared TiO<sub>2</sub>; (b and c) TEM images of anatase TiO<sub>2</sub>; (d) EDS pattern of as-prepared TiO<sub>2</sub>; (e) SAED image of anatase TiO<sub>2</sub>; (f) HRTEM image and FFT (inset) image of selected area from as-prepared TiO<sub>2</sub>.

**Fig.6.** (a) Initial three potential-capacity profiles of anatase TiO<sub>2</sub> nanowires at a charge/discharge current density of 20 mA g<sup>-1</sup>. (b) Representative cyclic voltammogram plot of anatase TiO<sub>2</sub> nanowires electrodes at 0.1 mVs<sup>-1</sup>.

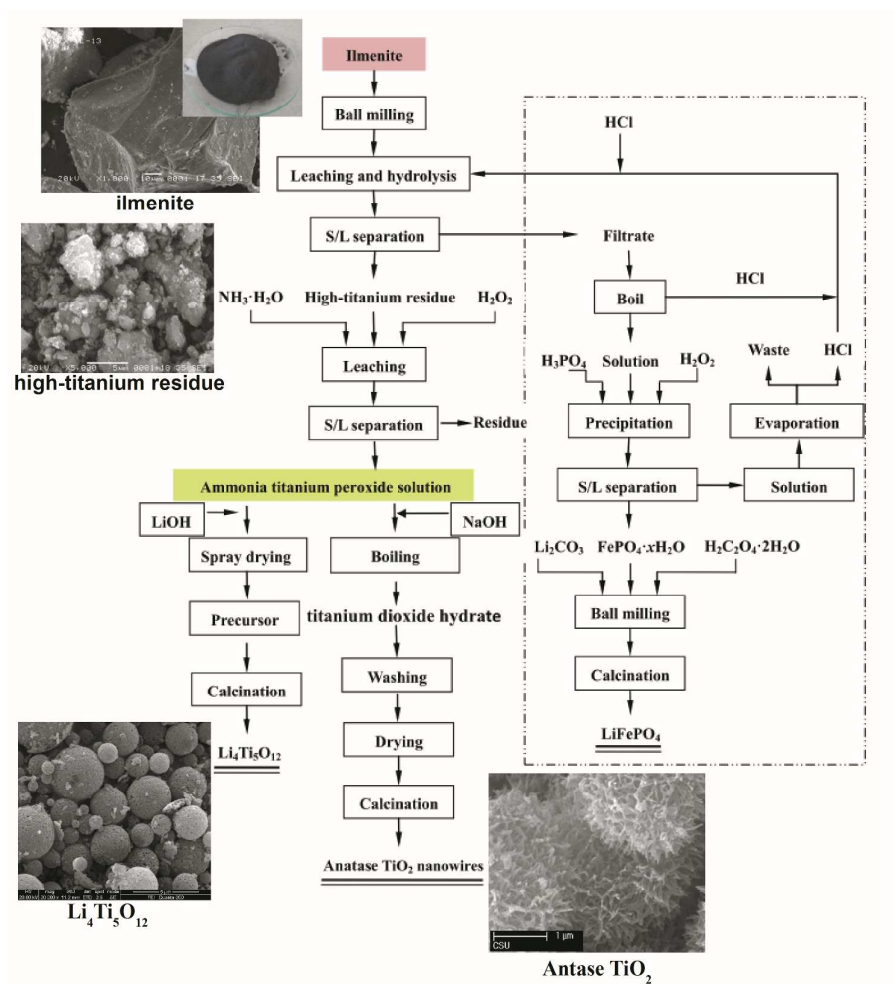
**Fig.7.** (a) Charge/discharge curves of anatase TiO<sub>2</sub> for multiple current densities in the voltage range of 1.0-3.0 V. (b) Cycling performance of anatase TiO<sub>2</sub> at multiple current densities. (c) Charge/discharge curves for the second and 288<sup>th</sup> cycles for TiO<sub>2</sub> at 20 mA g<sup>-1</sup>.

#### Table captions

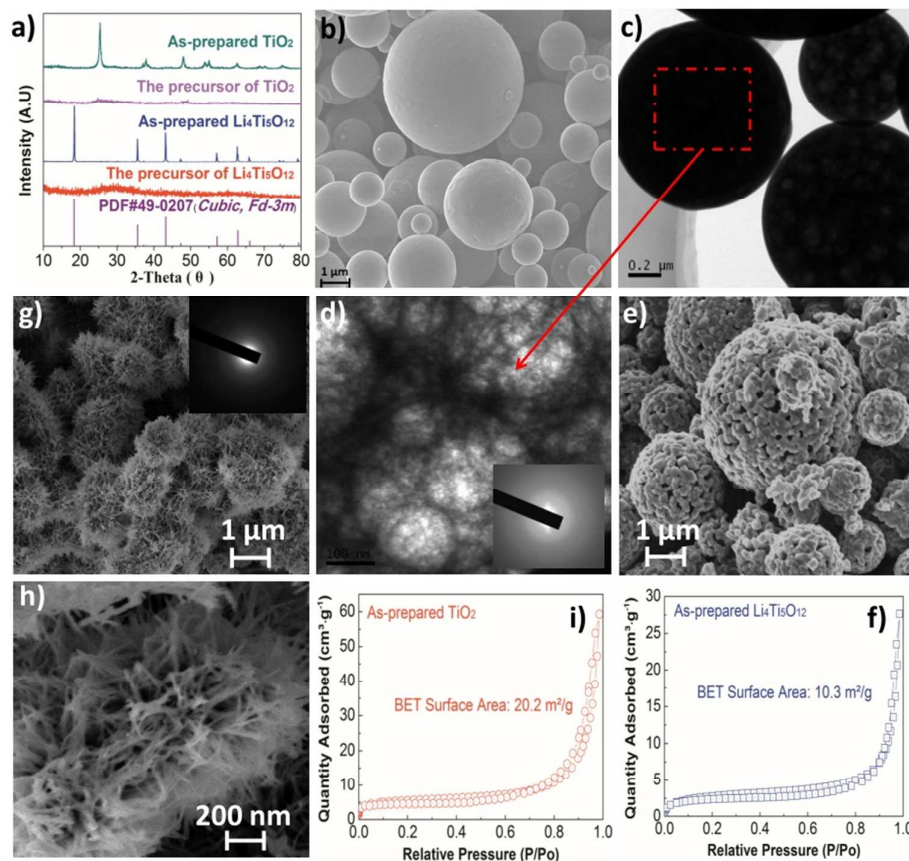
Table 1. Chemical composition of the ilmenite (wt.%).

Table 2. Comparison of electrochemical performance between Li<sub>4</sub>Ti<sub>5</sub>O<sub>12</sub> in this work and the previous Li<sub>4</sub>Ti<sub>5</sub>O<sub>12</sub> by the similar method using organic titanium compounds.

Table 3. Comparison of electrochemical performance between TiO<sub>2</sub> nanowires in this work and the previous TiO<sub>2</sub> nanowires by the similar method using organic titanium compounds.



**Fig.1** The detailed illustration of the synthesis process.



**Fig.2** (a) XRD patterns of the precursors and synthesized  $\text{Li}_4\text{Ti}_5\text{O}_{12}$  and  $\text{TiO}_2$ ; (b) SEM image of the precursor of  $\text{Li}_4\text{Ti}_5\text{O}_{12}$ ; (c and d) TEM images of the precursor of  $\text{Li}_4\text{Ti}_5\text{O}_{12}$  (inset: SAED pattern of the precursor of  $\text{Li}_4\text{Ti}_5\text{O}_{12}$ .); (d) The SEM image of as-prepared  $\text{Li}_4\text{Ti}_5\text{O}_{12}$ ; (g) SEM image and SAED (inset) of the precursor of  $\text{TiO}_2$ ; (h) SEM image of synthesized  $\text{TiO}_2$ . Physisorption isotherms for synthesized (i)  $\text{TiO}_2$  and (f)  $\text{Li}_4\text{Ti}_5\text{O}_{12}$ .

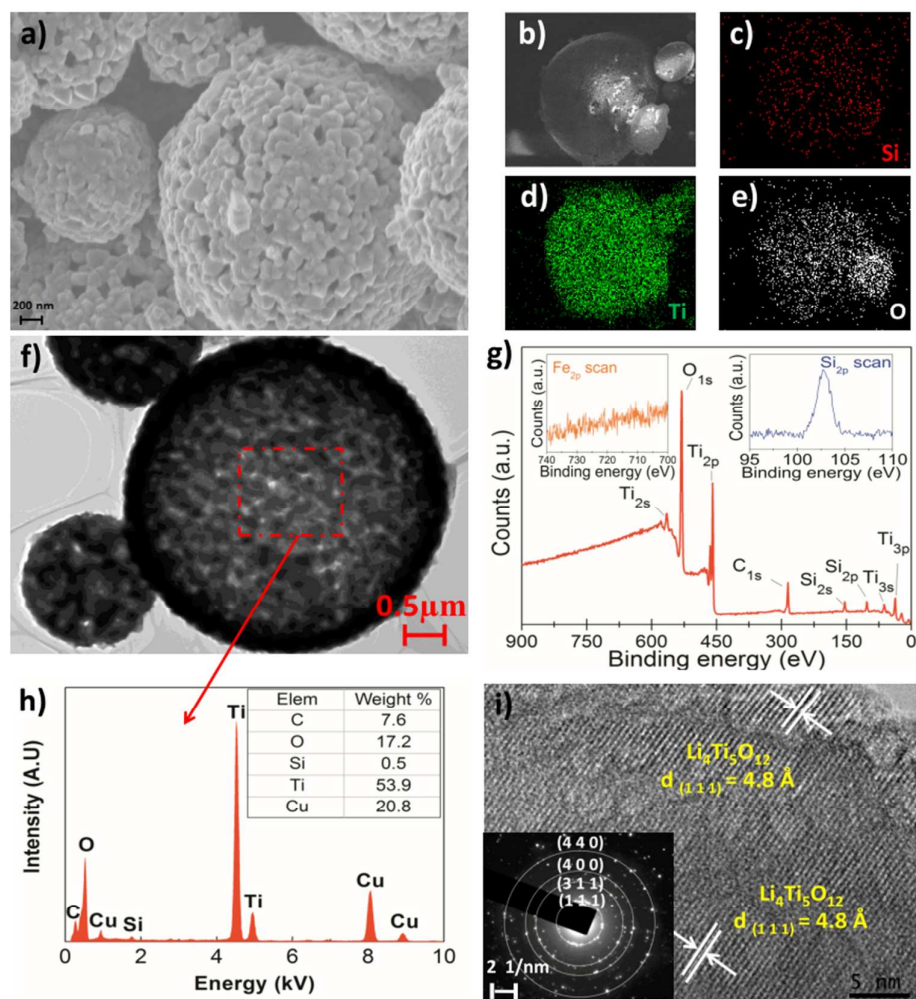


**Fig.3.** SEM (a), EDS mapping (b, c, d and e) and TEM (f) images of as-prepared  $\text{Li}_4\text{Ti}_5\text{O}_{12}$ ; (g) Typical XPS spectra of as-produced  $\text{Li}_4\text{Ti}_5\text{O}_{12}$  (The insets show high-resolution  $\text{Fe}_{2p}$  and  $\text{Si}_{2p}$  spectrums); (h) EDS pattern of selective area in TEM image; (i) HRTEM image and SAED (inset) image of as-produced  $\text{Li}_4\text{Ti}_5\text{O}_{12}$ .

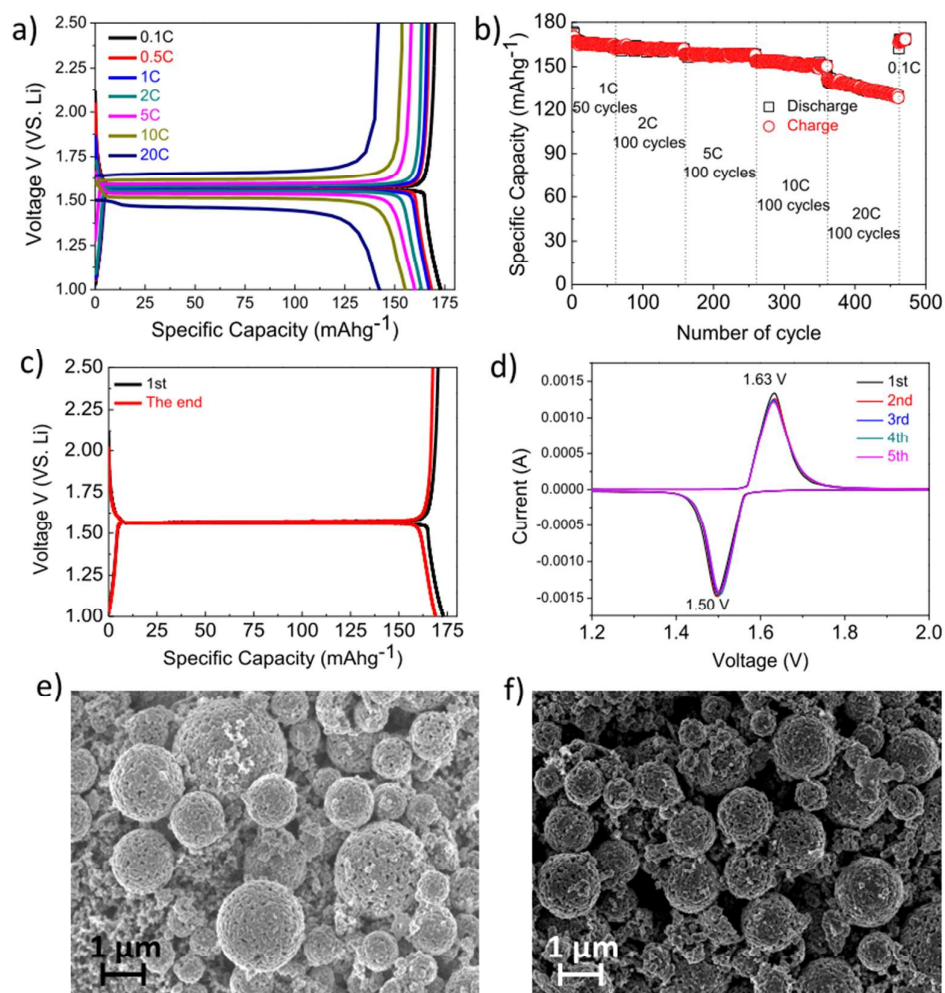


**Fig.4.** (a) Charge/discharge curves of  $\text{Li}_4\text{Ti}_5\text{O}_{12}$  at multiple C-rates in the voltage range of 1.0–2.5 V; (b) cycling performance of  $\text{Li}_4\text{Ti}_5\text{O}_{12}$  at multiple C-rates; (c) The first and 468<sup>th</sup> charge/discharge curves of  $\text{Li}_4\text{Ti}_5\text{O}_{12}$  at C/10 rate; (d) Cyclic voltammograms of the as-prepared  $\text{Li}_4\text{Ti}_5\text{O}_{12}$  at the scan rate of  $0.1 \text{ mVs}^{-1}$  between 2.5 and 1 V after charge/discharge testing; SEM images of as-produced  $\text{Li}_4\text{Ti}_5\text{O}_{12}$  electrodes (e) before and (f) after cycling.

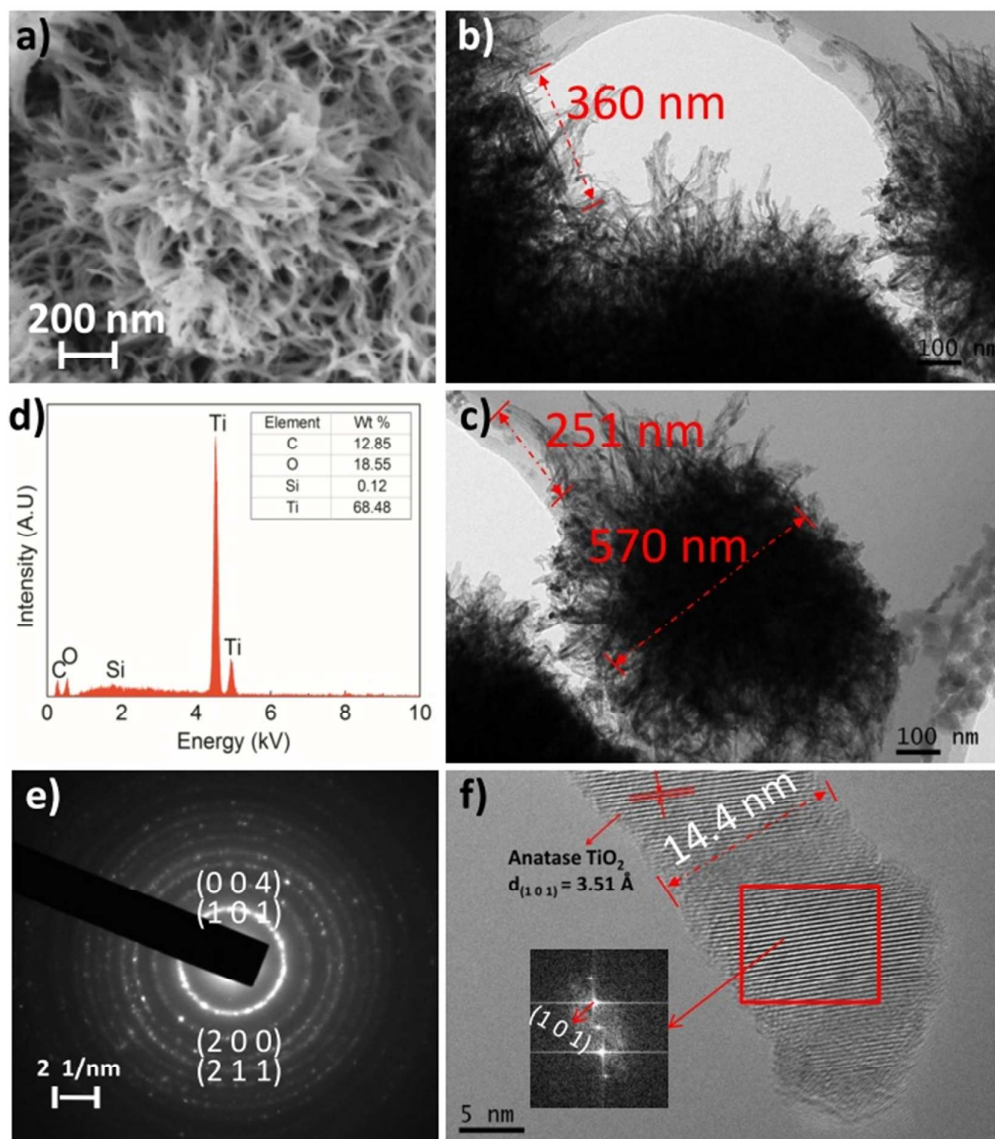


**Fig.5** (a) SEM image of as-prepared  $\text{TiO}_2$ ; (b and c) TEM images of anatase  $\text{TiO}_2$ ; (d) EDS pattern of as-prepared  $\text{TiO}_2$ ; (e) SAED image of anatase  $\text{TiO}_2$ ; (f) HRTEM image and FFT (inset) image of selected area from as-prepared  $\text{TiO}_2$ .

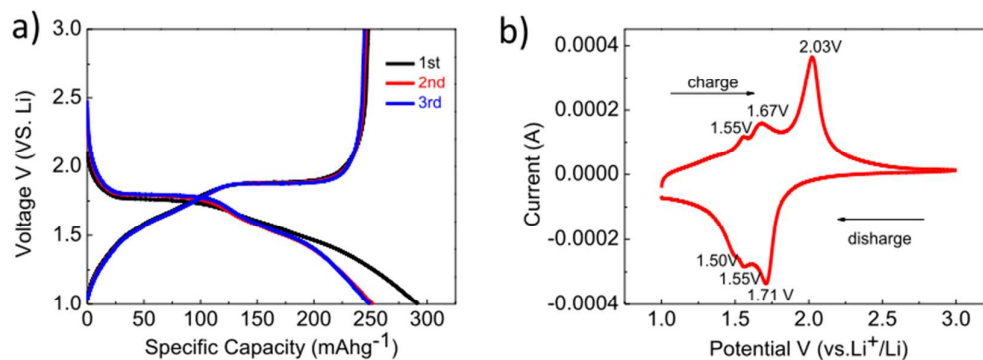


**Fig.6.** (a) Initial three potential-capacity profiles of anatase  $\text{TiO}_2$  nanowires at a charge/discharge current density of  $20 \text{ mA g}^{-1}$ . (b) Representative cyclic voltammogram plot of anatase  $\text{TiO}_2$  nanowires electrodes at  $0.1 \text{ mVs}^{-1}$ .

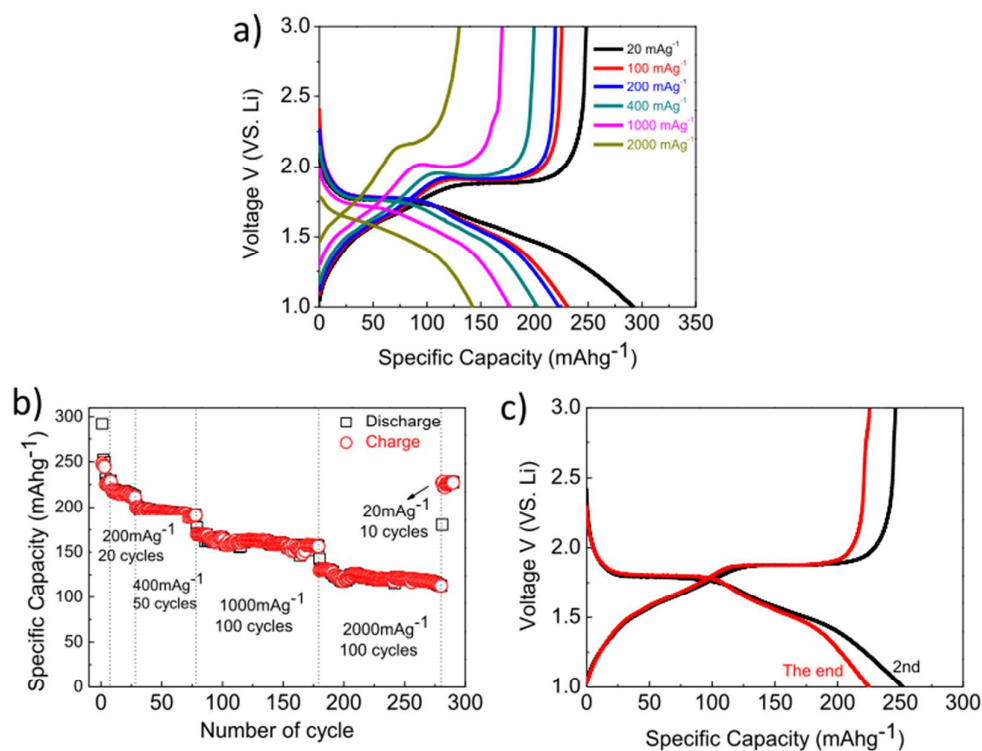


**Fig.7.** (a) Charge/discharge curves of anatase  $\text{TiO}_2$  for multiple current densities in the voltage range of 1.0-3.0 V. (b) Cycling performance of anatase  $\text{TiO}_2$  at multiple current densities. (c) Charge/discharge curves for the second and 288<sup>th</sup> cycles for  $\text{TiO}_2$  at  $20 \text{ mA g}^{-1}$ .